ACS APPLIED BIO MATERIALS

www.acsabm.org Article

Bioinspired Silk Fiber Spinning System via Automated Track-Drawing

Dave Jao, Xiao Hu, and Vince Beachley*

Cite This: *ACS Appl. Bio Mater.* 2021, 4, 8192–8204

Read Online

ACCESS | Metrics & More | Article Recommendations | Supporting Information

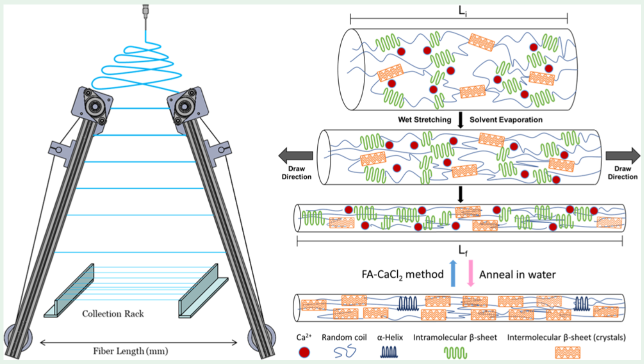

ABSTRACT: Regenerated silk fibroin (SF) fiber is a multifaceted protein matrix suitable for engineering a wide variety of biological materials. Numerous artificial spinning systems have been developed to mimic the molecular structure and hierarchical properties found in native silks. Here, we show a bioinspired technique that can readily form nanofibers and induce both orientation and structure formation of crystalline *β*-sheet assemblies seen in natural silk. In this study, electrospun postdrawn SF nanofibers were fabricated using an automated track-drawing (TD) approach for the continuous production of highly aligned protein nanofibers. This one-step postdrawing process simulates the dominant pulling force seen in natural spinning. The mechanical performance of the postdrawn SF nanofibers with a draw ratio of 2 (DR2) via TD exhibited a 115% increase in Young's modulus and an 80% increase in ultimate tensile strength, compared with the undrawn SF fibers after water treatment. It was also determined that the intermolecular *β*-sheet content in DR2 nanofibers increased by 75%. This contribution led to higher glass-transition and degradation temperatures. These biomimetic fibers with structural hierarchy and mechanical properties may be used to build high-performance load-bearing and directionally propagating structures relevant in biomaterial and sustainable material applications.

KEYWORDS: *silk, electrospinning, fibroin, postdrawing, nanofiber, β-sheet*

1. INTRODUCTION

The ability to spin and pull highly aligned silk fibroin nanofibers has great commercial, industrial, and scientific applications. Silk is a natural biomaterial possessing an exclusive combination of mechanical and physical properties such as high tensile strength, thermal stability, and high strain at breaking.[1] It is also considered one of the most promising green materials being biodegradable, biocompatible, bioinert, and renewable. Applications could range from super-thin sutures and scaffolds for surgery and wound dressings in biomedical engineering to fiber-reinforced composite materials in material and polymer engineering.[2,3] Efforts have been made to understand the flow conditions in natural silk spinning, which occurs at low temperatures and pressures, and to design the large-scale manufacturing of these natural fibers.[4] Currently, artificial silk fibers are made by traditional wet-spinning, which involves dissolving recombinant silk proteins in *N*-methyl morpholine *N*-oxide (NMMO), 1,1,1,3,3,3-hexafluoro-2-propanol (HFIP), trifluoroacetic acid (TFA), hexafluoroacetone (HFA), or 1-ethyl-3-methylimidazolium chloride and forcing the liquid feedstock through a die and exposing it in a coagulation bath to induce conformation transition and solidification.[5,6] Methanol and acetone baths have also been suggested as greener, cost-effective substitutes. However, these safer coagulants still severely degrade the silk fibroin (SF) and are toxic for use in cell-based applications. In addition, the coagulation rate at which SF forms is crucial to the behavior of the fiber during the drawing process, which will influence the mechanical properties of the fibers.[5] If the rate of transition is very slow, the fibers are not formed at all or form irregularly. On the other hand, if the coagulation rate is very rapid, such as in alcohols like ethanol, isopropanol, and methanol, the resulting fiber can become very brittle. In contrast, silkworms can solidify silk fibroin and sericin into a fiber at room temperature, leaving behind just water, causing less environmental damage. It has been suggested that if this process can be replicated in an industrial setting, it could improve how bioinspired and natural materials are processed and offer a more environmentally friendly alternative. In a recent study, Holland et al. have offered new insights into how *Bombyx mori* silkworm spin silk by exploring the effect of the

Received: May 28, 2021
Accepted: November 18, 2021
Published: December 1, 2021

https://doi.org/10.1021/acsabm.1c00630

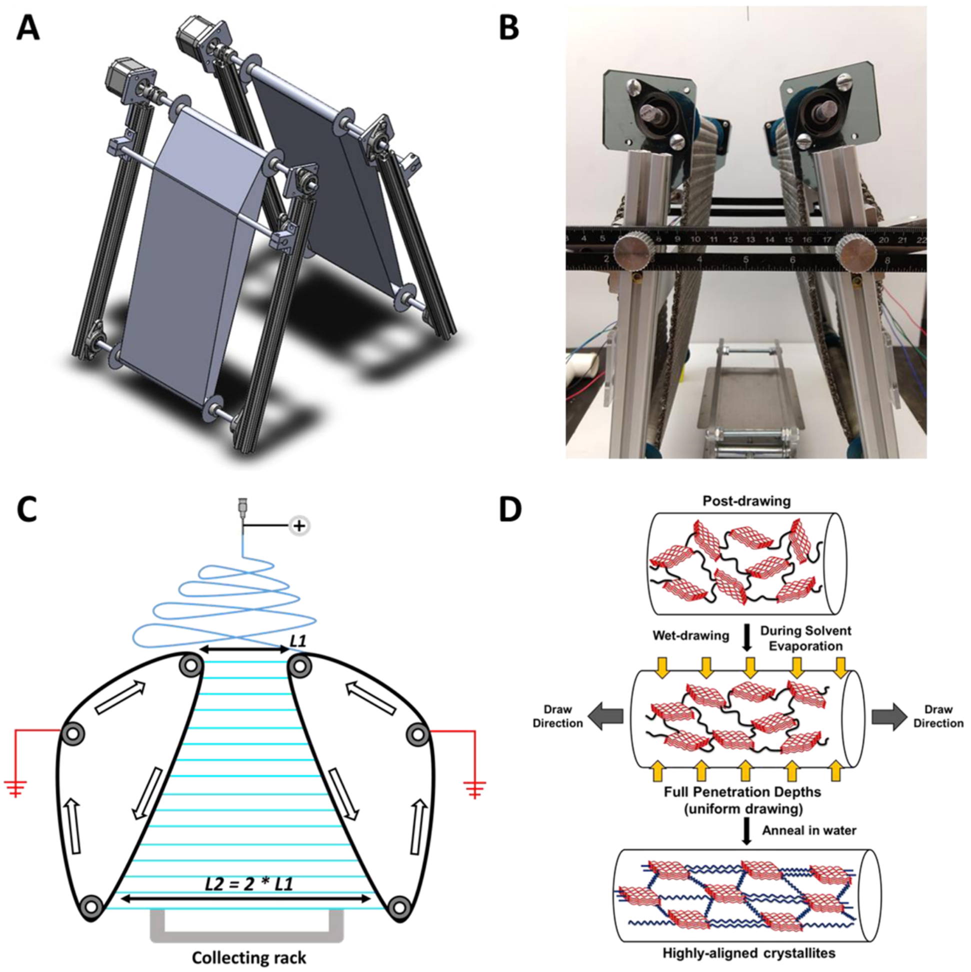

Figure 1. (A) Schematic illustration of the automated track-drawing (TD) apparatus. (B) Photograph of the automated TD system coupled with a parallel collection rack for producing highly aligned postdrawn silk fibroin (SF) nanofibers in ambient air. The draw ratio can be adjusted by modifying the track angle. (C) Diagram of the electrospinning postdrawing process. The automated TD system allows for the continuous postdrawing and collection of individual SF nanofibers. Electrospun nanofibers suspended over the top, initial gap of length (L1) between the rotating tracks were then postdrawn to a final length (L2) at the bottom of the tracks. As the uniaxially aligned nanofibers reach the bottom, a stationary rack or transparency sheet is present to collect the fibers in tension. Varying draw ratios of nanofibers can be obtained by simply changing the angle of the tracks. (D) Schematic illustration of the macromolecular alignment of postdrawn nanofibers during polymer−solvent evaporation and water annealing.

internal pressure of the silkworm during fiber production.[7] They concluded that the silkworm's body would not be able to contain the high pressure needed to squeeze itself hard enough to spin silk through extrusion alone. The study found that rather than being a conventional extrusion-based system where the material is forced through a die (a pushing mechanism), the silkworms predominantly spin their liquid silk feedstock dominated by a pultrusion effect (a pulling mechanism).[7]

Understanding how natural silks are spun in nature can lead to the unlocking of large-scale manufacturing of bioinspired products. To overcome current manufacturing difficulties and better mimic the mechanics of natural silk fabrication, we developed an automated track-drawing (TD) technique. This highly versatile spinning apparatus can produce highly aligned silk nanofibers with uniform sizes under ambient conditions. The automated TD design combines the discrete dry-spinning process with the vital postdrawing (pulling) process to mimic the pultrusion capability of the silkworm to pull fiber. In contrast to conventional wet-spinning approaches, the automated TD system is a first-stage, one-step drawing process. At the manufacturing level, the reduction of processing steps allows for easier fabrication and implementation of SF fibers in numerous applications that require tunable thermal and mechanical properties. The purpose of this study is to attain a better understanding of the silk postdrawing mechanism with respect to the β-sheet orientation behavior and to evaluate the differences between SF film, random, undrawn, and postdrawn nanofibers. Having increases in crystalline β-sheets within polymers is an advantageous trait for many applications, as it results in enhanced mechanical and thermal properties in the polymeric materials.[8] Understanding the orientation behavior of the β-sheet structure in highly aligned SF nanofibers is essential to revealing the microstructural change of silk during postdrawing that can offer remarkable material property enhancements in high-performance fibers (Figure 1D).

2. RESULTS

2.1. Preparation and Characterization. *2.1.1. Automated Track-Drawing System.* An automated TD process was developed and tested as a biomimetic approach to fabricate highly aligned SF nanofibers (Figure 1). The

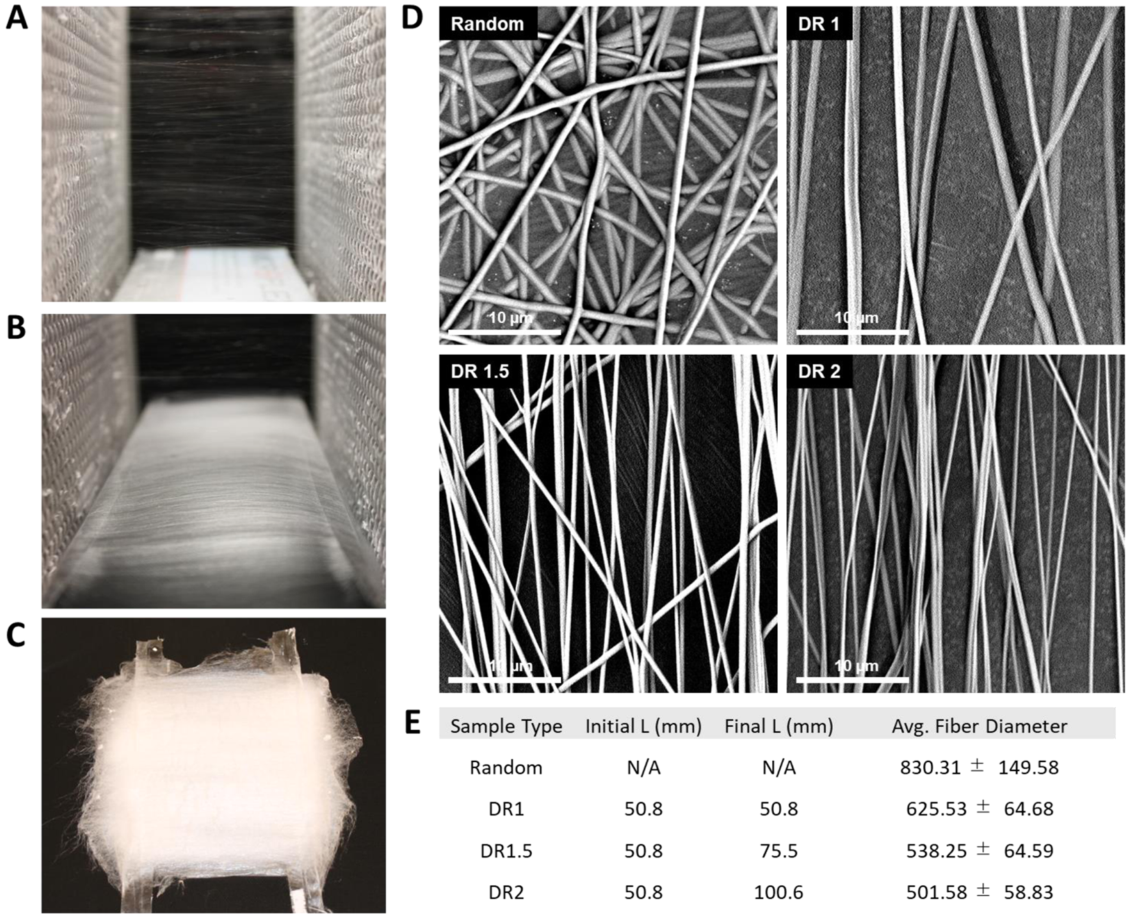

Sample Type	Initial L (mm)	Final L (mm)	Avg. Fiber Diameter
Random	N/A	N/A	830.31 ± 149.58
DR1	50.8	50.8	625.53 ± 64.68
DR1.5	50.8	75.5	538.25 ± 64.59
DR2	50.8	100.6	501.58 ± 58.83

Figure 2. (A) Photograph of individual electrospun SF postdrawn nanofibers suspended across two rotating tracks being stretched and drawn down the tracks for collection. (B) Photograph of thousands of uniaxially aligned nanofibers being continuously collected on a black sheet for contrast. (C) Photograph of highly aligned postdrawn SF nanofiber DR2 mat collected on a collection rack with the ability to control mesh size for tissue engineering and filtration applications. Nanofibers can be continuously postdrawn and deposited onto various collection frames or spools of complicated shapes and structures by tilting or angling the collection geometries. (D) SEM images show electrospun SF nanofiber morphology collected with the automated TD system for a draw ratio of 1 (undrawn), DR1.5, DR2, and random (control sample collected on a flat plate). (E) The table shows the postdrawn fiber lengths at the initial and final and the average fiber diameter per sample with the standard deviation ($n = 5$ independent fiber array samples). All scale bars = 10 μm.

schematic illustration of track-drawing and a photograph of the automated TD apparatus can be seen in Figure 1A−C. Positively charged electrospun fibers are deposited perpendicular to the two surfaces at the top of the track due to the electric field produced by a parallel plate style collector.[9] As the angled tracks rotate and move collected fibers away from the deposition area, the fibers are postdrawn and then collected. Through track-drawing, hundreds of individual electrospun nanofibers can be postdrawn simultaneously and collected onto a static collection rack, sheet, or fixture for analysis (Figure 2A,B). The TD apparatus consists of two rotating tracks that were angled at the top for the function of drawing nanofibers as they proceed down the widening bottom tracks.[10] Two stepper motors were employed to rotate the two grounded, stainless steel mesh tracks (Figure 1A−C). In this study, the draw ratio (DR = final fiber length/initial fiber length) between the bottom and the top tracks was set as 1:1, 1:1.5, and 1:2, designated as DR1 (undrawn), DR1.5, and DR2, respectively. At a draw ratio DR3, fiber breakage was observed. Optimization of parameters may facilitate higher draw ratios prior to breakage in future work. For all TD collections, the initial track gap length was fixed at 5 cm and the final track gap length was adjustable to 10 cm to examine the structural changes for a broad range of draw ratio (DR1 = 5 cm, DR1.5 = 7.5 cm, and DR2 = 10 cm). The effect of postdrawing conditions on the structure and properties of electrospun SF nanofibers was investigated by varying the first-stage draw ratio during the semisolid state before complete solvent evaporation and collection. Five samples ($n = 5$) of each condition were collected and mounted on plastic frames measuring 1 cm by 1 cm for structural analysis, which included random mesh (control), draw ratio = 1 (DR1, undrawn), draw ratio = 1.5 (DR1.5), draw ratio = 2 (DR2) nanofibers, and film samples. For this study, the stepper driver was set to a 1.8° stepper with a 1/8 microstepping, which equates to 1280 steps/mm, and the stepper motor was mounted directly to an M8 aluminum rod using a 5−8 mm aluminum collar. The track speed (mm/s) was adjusted using a programmable stepper motor controller to fix the linear silk fiber draw rate at 4.22 mm/s.

2.1.2. Structure and Appearance of Highly Aligned Postdrawn Nanofibers. Morphological changes of the as-spun and postdrawn SF nanofibers were observed by SEM. The scanning electron micrographs of electrospun random (control), DR1 (undrawn), DR1.5, and DR2 SF nanofibers are shown in Figure 2D. From the SEM images, all electrospun SF

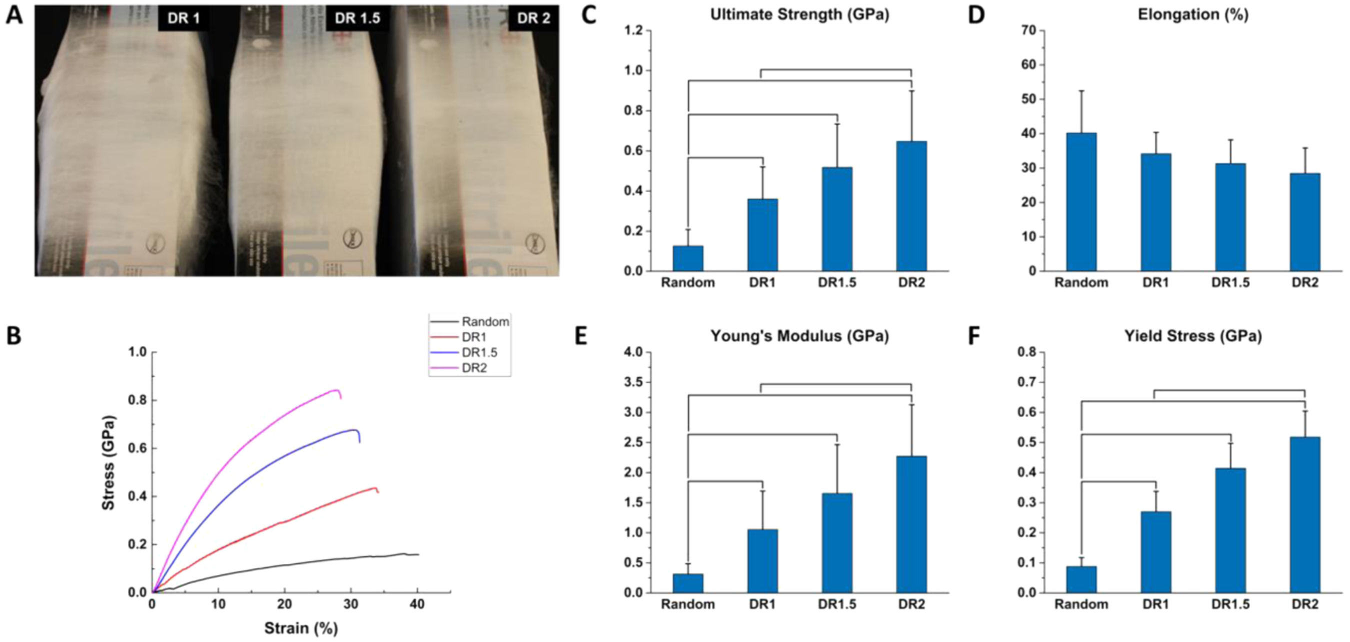

Figure 3. Mechanical properties of electrospun and postdrawn SF nanofibers. (A) Photograph of DR1, DR1.5, and DR2 electrospun SF nanofiber mats. (B) Stress−strain curves for random mesh (control), DR1 (undrawn), DR1.5, and DR2 SF nanofibers. (C−F) Ultimate tensile stress, elongation at break, modulus of elasticity, and yield stress were calculated from the stress−strain curves ($n = 5$). The connected lines denote statistically significant differences obtained from the Mann−Whitney analysis of all group-to-group comparison, $P < 0.05$.

nanofibers exhibited a uniform and smooth fiber structure without beading or necking. Nanofibers collected with the automated TD apparatus demonstrated a predominantly well-aligned orientation, while nanofibers obtained on a static aluminum plate had large variations of orientation in all directions. The SF random nanofibers showed a slight undulating (wavelike) shape, with no beading or pitting. For the parallel spun nanofibers, SEM images showed predominantly smoother and straighter fiber structures than the random as-spun nanofibers. Postdrawing nanofibers, especially at high draw ratios, did seem to improve the overall fiber alignment and structure. No apparent cracks, granules, or irregular voids on the fiber surface were found in all of the postdrawn nanofibers. The average fiber diameters of the electrospun SF nanofibers are shown in Figure 2E. As the fibers are drawn from DR1 to DR2, the average diameter of the fiber showed an overall reduction from 626 to 502 nm. The diameter reduction resulting from fiber thinning with fiber elongation followed the predicted conservation of volume model closely.

With the continuous mechanized collection and in-line stretching of electrospun nanofibers, the automated TD allows for thousands of fibers to be postdrawn simultaneously with high consistency. Generally, as the fibers are lengthened to higher DR, the surface of the drawn fibers became smoother, as the rough and bumpy surfaces disappear. The influence of drawing and the plasticization (molecular mobility) by $CaCl_2$ allow the entangled globular and fibrillar physical structures in the postdrawn SF fiber to straighten, resulting in more uniform fibers. Subsequently, to remove the calcium and chloride ions in the regenerated SF nanofiber, which inhibits the assembly of β-sheets, nanofibers were soaked in DI water. Established in previous studies, the immersion of SF in water or alcohol-based coagulants has shown to increase the β-sheet content in the nanofiber.[11−13] During this annealing (soaking) process, protein molecules can reorient and reassemble. With improved realignment and intermolecular interaction of the interbackbone hydrogen-bonding networks, major improvements can be seen in the material rigidity and mechanical properties.

2.2. Mechanical Properties. The mechanical properties of as-spun and postdrawn SF nanofibers with increasing draw ratios were tested. Figure 3B plots the typical strain−stress curves of the drawn and undrawn SF nanofibers. Figure 3C,D shows the tensile strength, Young's modulus, yield stress, and breaking elongation derived from stress−extension curves. The results indicate that tensile moduli and strengths are increased as fibers are drawn at greater lengths using the TD system. A tensile strength value of 0.64 GPa obtained for the DR2 sample was markedly higher than those obtained by DR1.5 and DR1 (undrawn). Between the undrawn samples, as-spun random SF nanofibers showed the lowest tensile strength with 0.12 GPa. On comparing DR1 to DR2, there was a 115% increase in Young's modulus from 1.05 to 2.27 GPa and an 80% increase in the ultimate tensile strength from 0.36 to 0.65 GPa. In a similar manner, an overall 85% increase in yield stress was also observed from DR1 (0.30 GPa) to DR2 (0.56 GPa) samples. It should be noted that there is a trade-off between tensile strength and elongation at break with an overall reduction in elongation at failure from random to DR2 at values of 40 and 28%, respectively. The mechanical properties of drawn fibers are greater than those of undrawn fibers, which can be attributed to the degree of molecular orientation and parallel arrangement of aggregated secondary structures, which leads to less slippage of chains under loading. As the fiber is drawn down and lengthened, the physical arrangements of the amorphous and crystalline regions become more ordered, and the physical interactions among polymer chains and secondary structures become untangled and more closely arranged.

2.3. FTIR Analysis. Infrared spectroscopy was used to characterize the conformational transitions in the secondary structures of SF after postdrawing. FTIR absorbance spectra

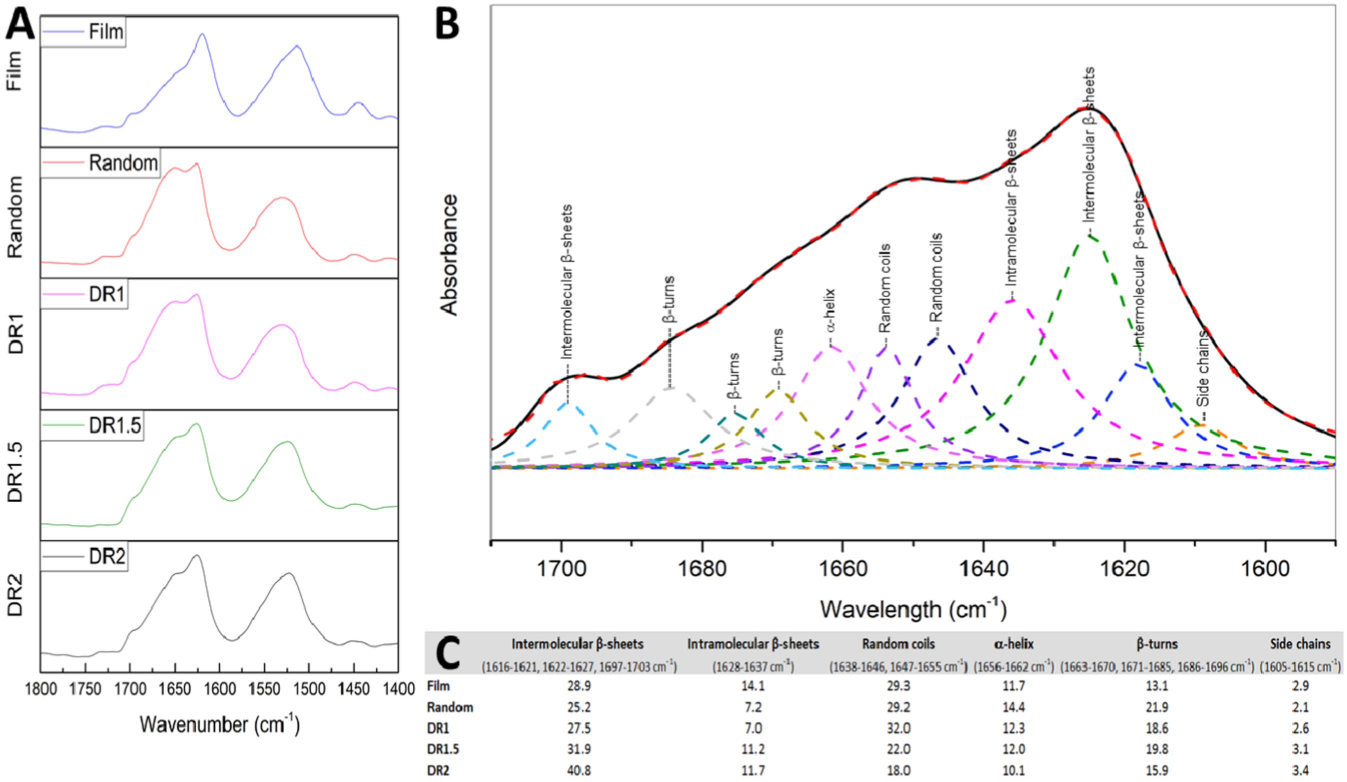

	Intermolecular β-sheets (1616-1621, 1622-1627, 1697-1703 cm^{-1})	Intramolecular β-sheets (1628-1637 cm^{-1})	Random coils (1638-1646, 1647-1655 cm^{-1})	α-helix (1656-1662 cm^{-1})	β-turns (1663-1670, 1671-1685, 1686-1696 cm^{-1})	Side chains (1605-1615 cm^{-1})
Film	28.9	14.1	29.3	11.7	13.1	2.9
Random	25.2	7.2	29.2	14.4	21.9	2.1
DR1	27.5	7.0	32.0	12.3	18.6	2.6
DR1.5	31.9	11.2	22.0	12.0	19.8	3.1
DR2	40.8	11.7	18.0	10.1	15.9	3.4

Figure 4. (A) FTIR absorbance spectra of electrospun DR1- (undrawn), DR1.5-, DR2-, random-, and film-regenerated SF samples. (B) Fourier self-deconvolution (FSD) amide I spectra with curve fitting for postdrawn DR2 SF nanofibers. The dashed lines represent the fitted peaks, the red dashed curve represents the summed peaks, and the black solid curve represents the original spectra. (C) The table shows the percentages of secondary structures in various regenerated SF nanofibers and film samples calculated by an FTIR deconvolution method.

were analyzed as a function of draw ratio in the frequency range 1800−1400 cm^{-1} for electrospun DR1, DR1.5, and DR2 nanofiber samples shown in Figure 4 using previously described methods.[14−16] In addition, the infrared spectra of SF film and random mesh samples are also shown. According to numerous studies, the FTIR spectrum of SF has strong absorption bands between 1700 and 1500 cm^{-1} that refer to the absorption of the peptide backbones in the region 1700−1600 cm^{-1} for amide I and 1600−1500 cm^{-1} for amide II.[17−19] Generally, the amide I peak positions at 1610−1623 cm^{-1} (*β*-sheet conformation) and 1640−1654 cm^{-1} (random coil conformation) corresponds to the C═O stretching vibrations of the protein backbones. In contrast, the amide II absorption bands at 1510−1520 cm^{-1} (*β*-sheet conformation) and 1535−1545 cm^{-1} (random coil conformation) are attributed to the side-chain groups and out-of-phase vibrations from the C−N stretching and the N−H in-plane bending.[20,21] These two major regions are typically used for the structural and quantitative analyses of silk I and silk II secondary structures.

After post-treatment with water annealing, electrospun SF DR1.5 and DR2 nanofibers and film samples showed high absorption intensities in the amide I and amide II regions, indicating the presence of secondary protein structures (Figure 4A), while electrospun SF DR1 and random mesh nanofibers showed more broadening peaks. For the water-treated SF film in the amide I region, the peak position has shifted to 1620 cm^{-1} (from 1640 cm^{-1}), while for SF nanofibers, the peak was centered around 1626 cm^{-1} indicating the presence of an intermolecular *β*-sheet crystal structure. Whereas the water-treated SF film in the amide II region was shifted to 1513 cm^{-1} (from 1520 cm^{-1}), the SF nanofibers were centered around 1523 cm^{-1}. To find the percentage secondary structure in regenerated SF samples, a quantitative analysis of the amide I band was calculated using the FSD fitting method. To clarify, an example of the FSD curve-fitting method on the amide I region of DR2 (drawn) nanofiber is shown in Figure 4B. FSD curve-fitting examples for SF random (control), DR1 (undrawn), DR1.5 (drawn), and film (casted) samples are shown in Figure S2. In Figure 4C, the table shows the percentages of secondary structures in SF film and nanofiber samples calculated from the second derivative and the area of each fitted peak in the amide I spectra. A significant increase in intermolecular *β*-sheets from 17.4% DR1 (undrawn) to 30.5% postdrawn DR2 was observed, as well as a slight increase in intramolecular *β*-sheets from 17.2 to 22.0%, respectively. Meanwhile, the random coil content of undrawn DR1 SF nanofibers showed a decrease from 32.0 to 18.0% postdrawn DR2 during the postdrawing and FA regeneration (annealing) process. Postdrawn DR1.5 SF nanofibers also followed a similar pattern, with improvements in intermolecular and intramolecular *β*-sheet contents. No significant differences between the random mesh (control) and DR1 (undrawn) SF nanofibers were observed in the intermolecular *β*-sheet content, except for a minor variation in the intramolecular *β*-sheet content.

The characteristic FTIR absorbance spectra of the amide I and amide II bands allow us to follow the crystalline phase conformational transitions and determine the secondary structure content induced mechanically and by dehydration process in the SF nanofiber and film samples. Using the FTIR deconvolution method, SF DR2 nanofibers showed relatively higher crystallinity and crystalline orientation, while random

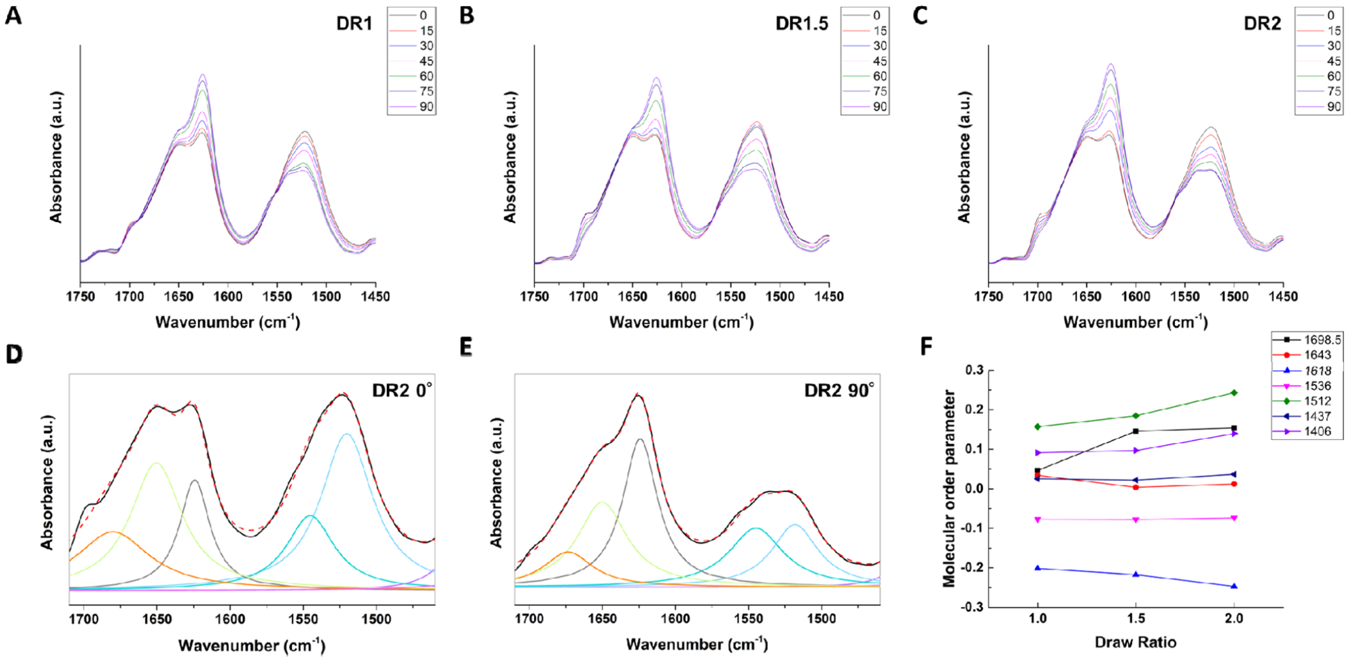

Figure 5. (A−C) Polarized FTIR spectra of electrospun DR1- (undrawn), DR1.5-, and DR2-regenerated SF nanofibers obtained with the electric field at different angles with respect to the fibers, 0 (electric field is parallel to the fiber), 15, 30, 45, 60, 75, and 90° (electric field is perpendicular to the fiber). (D, E) A joint amide I and II curve-fitting example for the polarized FTIR spectra of postdrawn DR2 SF nanofibers from 1725 to 1425 cm^{-1} recorded at 0 and 90°. The black solid curve represents the original spectra, the colored solid lines represent the fitted peaks, and the red dashed curve represents the summed peaks. (F) Plot of polarized FTIR-derived molecular order parameters $\langle P_2 \rangle$ of 1698.5 ± 1, 1643 ± 4, 1618 ± 2, 1536 ± 1, 1512 ± 3, 1437 ± 1, and 1406 ± 1 cm^{-1} components for DR1, DR1.5, and DR2 SF nanofibers.

mesh nanofibers were more amorphous. A detailed structure assessment can be found in Figure 4C, listing the contents of secondary structures. From the table, the *β*-sheet content of postdrawn DR2 was 52% higher compared to that of DR1 (undrawn) SF nanofibers. In comparison, the total *β*-sheet content of random mesh (control) and DR1 (undrawn) SF nanofibers does not have noticeable changes. Also, the intermolecular *β*-sheet content of postdrawn DR1.5 was equally as high as that of DR2 compared to undrawn nanofibers. As the automated tracks draw down electrospun nanofibers, shearing and elongational forces cause strands of protein to come in close proximity, leading to the orientation of crystalline and molecular structures along the stretched direction. This molecular movement of the amorphous regions allows for the formation and generation of silk II structure (*β*-sheet secondary structure) and reorganization of intermolecular hydrogen bonds in the fibril bundles of drawn silk fibers after water treatment. Therefore, the automated TD approach can promote the formation of oriented *β*-sheets. Thus, these microstructure changes result in the construction of more rigid nanofibers, which also correspond to the mechanical analysis.

2.4. Structural and Orientation Changes Induced by Postdrawn Treatments of Fibers. To evaluate the changes in polymer backbone orientation with postdrawing, polarized Fourier transform infrared spectroscopy (FTIR) was used to examine the amide groups of the SF nanofibers. Polarized FTIR provided an effective way to study the orientation behavior of *β*-sheet crystallites. The schematic diagram for the acquisition of 0 and 90° spectra is shown in Figure S1. For degummed silk, it is mainly composed of fibroin, which mostly consists of antiparallel *β*-sheet crystallites and random coil (amorphous) regions.[22] The *β*-sheet crystallites of fiber are recognized as an orthorhombic or monoclinic unit cell (γ = 86°), with a = 0.944 nm for the interchain direction (hydrogen bonding), b = 0.895 nm for the intersheet direction, and c = 0.700 nm for the fiber axis direction.[23,24] *β*-Sheet crystallites are highly organized and predominantly orientated parallel to the natural silk fiber axis.[25] The *β*-sheet crystallites are generally formed by the alanine-rich and glycine-rich polypeptide chains, while hydrogen bonds assemble the chains in an antiparallel arrangement.[26,27] There are amide groups in the backbone of *β*-sheets that contribute to amide bands in infrared spectroscopy. The amide I band is dominated by the C═O stretching vibration, and its transition moment is nearly perpendicular along the *β*-sheet backbone,[23] while the amide II band is predominated by the N−H in-plane bending and C−N stretching vibrations (C−N−H vibrations for short) and both approximately parallel to the *β*-sheets (Figure S1). By differentiating between amide I and amide II bands, the orientation behavior of the *β*-sheets can be obtained by investigating the orientation degree of C═O and C−N−H transition moments.[23] The molecular order parameter of *β*-sheet precursors in amide II (approximately at 1515 cm^{-1})[28] and the molecular orientation component of *β*-sheet crystalline in amide I at 1616 cm^{-1} could be markers to reveal the molecular evolution associated with the postdrawing of SF.

From the polarized FTIR spectra (Figure 5A−E), the most intense bands with dichroic properties are the amide I and II vibrations with absorption bands between 1700 and 1500 cm^{-1}. Changes in the dichroic ratio for the carbonyl (C═O) stretching vibration of the *β*-sheets at wavelength 1620 cm^{-1} were observed with an increasing draw ratio. The carbonyl absorption intensities for SF nanofibers collected on the TD apparatus were greater when the FTIR beam was polarized perpendicular to the fiber axis, suggesting that the carbonyl is more aligned normally with the direction of the silk fiber axis at

Table 1. Assignment, Percentage, Preferential Orientation, and Conformational Transition in the Secondary Structure of SF Obtained from Joint Amide I and II Curve Fitting of the Polarized ATR Spectra[a]

	wavenumber (cm^{-1})		conformation structure	FWHM (cm^{-1})		relative area (%)		preferential orientation	$\langle P_2 \rangle$
DR1	0	90°		0°	90°	0°	90°		
	1699	1698	β-sheets	60	47	13.19	11.52	∥	0.05
	1639	1647	random coil	44	42	24.14	21.82		0.03
	1616	1620	β-sheets	25	29	12.25	24.69	⊥	−0.20
	1536	1536	random coil$^{\mu}$	40	45	12.60	16.03		−0.08
	1513	1511	β-sheets$^{\omega}$	43	41	29.90	19.17	∥	0.16
	1437	1437	side chain	33	30	4.38	4.06	⊥	0.03
	1406	1406	side chain	47	42	3.53	2.71	∥	0.09
DR1.5	0°	90°		0°	90°	0°	90°		
	1699	1698	β-sheets	61	43	14.56	9.63	∥	0.10
	1639	1647	random coil	42	43	22.92	22.67		0.00
	1616	1620	β-sheets	25	29	12.52	26.96	⊥	−0.22
	1536	1536	random coil$^{\mu}$	40	46	13.11	16.74		−0.08
	1513	1511	β-sheets$^{\omega}$	43	41	29.08	17.31	∥	0.18
	1437	1437	side chain	33	29	4.30	4.02	⊥	0.02
	1406	1406	side chain	48	43	3.52	2.66	∥	0.10
DR2	0°	90°		0°	90°	0°	90°		
	1699	1698	β-sheets	61	41	13.96	9.02	∥	0.15
	1639	1647	random coil	43	41	23.39	22.57		0.01
	1616	1620	β-sheets	25	29	12.50	28.82	⊥	−0.25
	1536	1536	random coil$^{\omega}$	40	46	13.02	16.39		−0.09
	1513	1511	β-sheets$^{\omega}$	43	39	29.14	14.84	∥	0.24
	1437	1437	side chain	34	29	4.38	3.93	⊥	0.04
	1406	1406	side chain	48	43	3.61	2.43	∥	0.14

[a] Abbreviations: μ, amide II unordered (amorphous); ω, β-sheet related, water-inaccessible (C−C) stretching and (CH) bending, tyrosine.

90°. While the peak at 1510 cm^{-1} related to the vibrations of N−H bending and C−N stretching of the β-sheets showed greater absorption intensities at 0°, indicating that the C−N−H is more aligned parallel to the silk fiber axis with maximum absorbance at the parallel absorption. Since the transition moment of C═O is rigid and perfectly aligned perpendicular to the polymer chain backbone at a right angle (90°), a correction is not needed to determine the dichroic ratio for a polymer backbone with optimal orientation in the direction of the fiber axis. An example of the decomposition of both amide bands was employed to obtain quantitative information on the orientation structure of silk nanofiber.[23,29,30] The spectra deconvolution results of postdrawn DR2 SF nanofibers at 0 and 90° are shown in Figure 5A−E. For joint amide I and II, curve-fitting examples of undrawn DR1 and postdrawn DR1.5 SF nanofibers from 1725 to 1425 cm^{-1} recorded at 0 and 90° can be found in Figure S3. More details about the position, assignment, and the value of the molecular order parameter $\langle P_2 \rangle$ of the individual band are given in Table 1.

The component within 1620−1616 cm^{-1} was assigned to β-sheets, and 1513−1511 cm^{-1} was considered to be the combination of water-inaccessible and water-accessible β-sheets (interphase β-sheets).[23,31] The peaks at 1647−1639 and 1536 cm^{-1} belong to the random coils, and the peaks at 1437 and 1406 cm^{-1} belong to the side chain in previous studies.[32] Additionally, the 1699−1698 cm^{-1} component was assigned to weak β-sheets and β-strands. From Table 1, the crystalline β-sheets of drawn DR2 nanofibers have shown to be slightly more orientated along the fiber axis, with $\langle P_2 \rangle$ value of −0.25 for 1620−1616 cm^{-1} component and the amorphous region (random coil) with $\langle P_2 \rangle$ close to zero showed no orientation. The molecular order parameter of the 1513−1511 cm^{-1} band is also slightly higher, with a value of 0.24 compared to the undrawn of 0.16. After drawing, the $\langle P_2 \rangle$ for amide I (1513−1511 cm^{-1}) exhibited a more positive value indicating an increase in parallel alignment along the fiber axis, while the $\langle P_2 \rangle$ for amide II (1620−1616 cm^{-1}) showed a more negative value indicating that the polymer side chains were oriented toward the perpendicular direction of the fiber axis, suggesting an overall improvement in the alignment of crystalline β-sheets. The $\langle P_2 \rangle$ value calculated from 1699 to 1698 cm^{-1} presented a higher value from 0.05 (DR1) to 0.15 (DR2), which indicated a higher degree of orientation parallel to the fiber axis. To help visualize the details, the assignment and the value of molecular order parameter $\langle P_2 \rangle$ of each band are plotted against the draw ratio in Figure 5F. Given the results of the crystalline β-sheet content and changes in dichroic ratio, this indicates that the orientation of the molecular protein chains of DR2 is promoting the formation of ordered β-sheet structures along the fiber axis. While the effect is limited, the orientation of molecular chains evidently showed increases for drawn nanofibers.

2.5. Thermal Analysis.

In addition to enhanced mechanical properties, the postdrawing process has led to remarkable changes in the formation of hierarchical structures in the SF nanofibers, which directly affects the thermal behavior of the fiber. Standard DSC and temperature-modulated DSC (TMDSC) measurements were performed to evaluate the phase behavior and influence of TD on the thermal properties of the postdrawn SF nanofibers. The melting endotherms obtained for the various SF nanofibers at different draw ratios and film samples are shown in Figure 6. During the initial heating scans, DSC thermograms of SF film, random, DR1 (undrawn), and DR1.5 (drawn) nanofibers displayed a noticeable single endothermic peak associated with the typical low-boiling bound solvent evaporation peak (T_{d1})

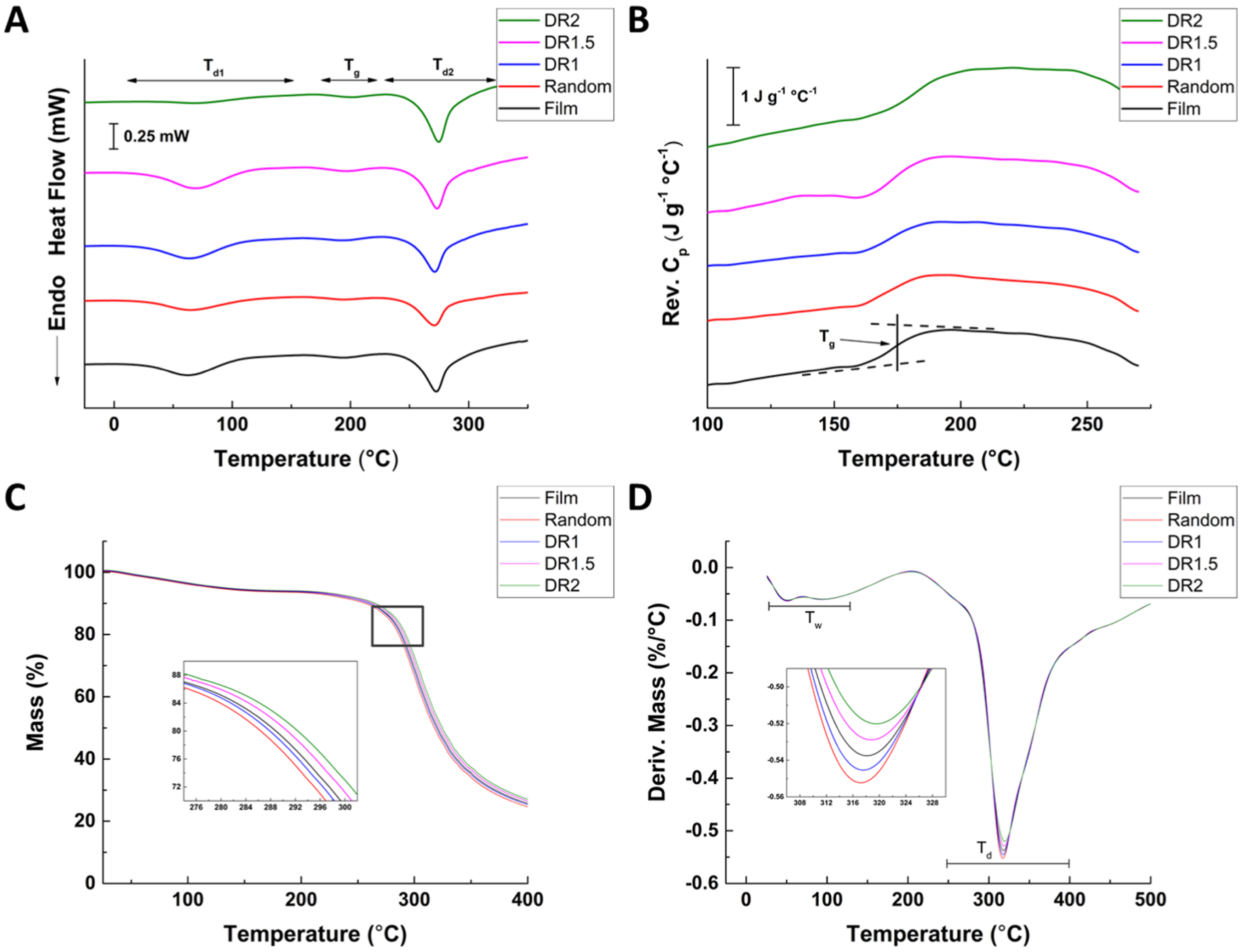

E

silk sample	T_g/° C	ΔC_p at T_g / J g^{-1} K^{-1}	solvent release T_{d1}/° C	degradation temp T_{d2}/° C	onset temp of decomposition/° C	bound solvent content/%	degradation middle temp T_{dm}/° C	remaining mass at 400° C/%
Film	175.28	0.59	63.15	273.06	286.47	9.85	318.11	26.48
Random	173.68	0.50	66.03	270.86	284.54	9.92	317.25	24.58
DR1	174.30	0.49	64.42	271.67	285.74	9.88	317.42	26.37
DR1.5	177.11	0.65	67.36	273.15	287.07	9.76	318.81	26.55
DR2	182.07	0.80	65.63	273.65	288.47	9.72	319.68	26.71

Figure 6. (A) Standard DSC scans of electrospun DR1- (undrawn), DR1.5-, DR2-, random-, and film-regenerated SF samples, with temperatures corresponding to bound solvent evaporations (T_{d1}), glass transitions (T_g), and sample degradations (T_{d2}). (B) TMDSC measurement for the reversing heat capacities of the SF fibers and film samples. (C) Thermogravimetric analysis curve representing the percent mass remaining of electrospun DR1- (undrawn), DR1.5-, DR2-, random-, and film-regenerated SF samples. (D) The first derivative of the TGA curve (DTG) representing the degradation rates of the SF fibers and film samples with temperature degradations (T_d) and temperature water evaporations (T_w). (E) The table shows the T_g, ΔC_p at T_g, T_{d1}, and T_{d2} by DSC and TMDSC analyses and the onset temperature, T_{dm}, percentage of bound solvent, and mass remaining by TGA and DTG for random, DR1, DR1.5, DR2, and film SF samples.

in the 60−100 °C (333−373 K) temperature range. For temperatures after the T_{d1} region, the baseline in all DSC scans remains relatively flat until reaching the glass-transition temperature (T_g) region and, lastly, the degradation temperature (T_{d2}) region as depicted in Figure 6A. To investigate the reversible thermal properties of the SF materials near the T_g regions, the heat capacity increases (ΔC_p) were determined from their respected TMDSC curves in Figure 6B. From the TMDSC curves, all SF samples showed clear ΔC_p relative to their T_g regions. The results (T_g and ΔC_p) obtained from the DSC thermograms are listed in Figure 6E. Subtle changes were found in the glass-transition temperature of drawn and undrawn SF samples, with increases in draw ratio showing a T_g trend of random < DR1 < film < DR1.5 < DR2. It should be noted that the T_g value of the SF film was slightly higher than those of SF random and DR1 (undrawn) samples. Consequently, the heat capacity increments ΔC_p at T_g of drawn SF nanofibers are also higher than those of undrawn nanofibers and film samples, with a ΔC_p trend of DR1 < random < film < DR1.5 < DR2. The ΔC_p is inferred as the average chain mobility of the SF protein secondary structures that gives an indirect measurement reflecting the number of freely rotating bonds on the chain conformation.[22] From the DSC results, the effect of draw ratio on the thermal behavior suggests that the

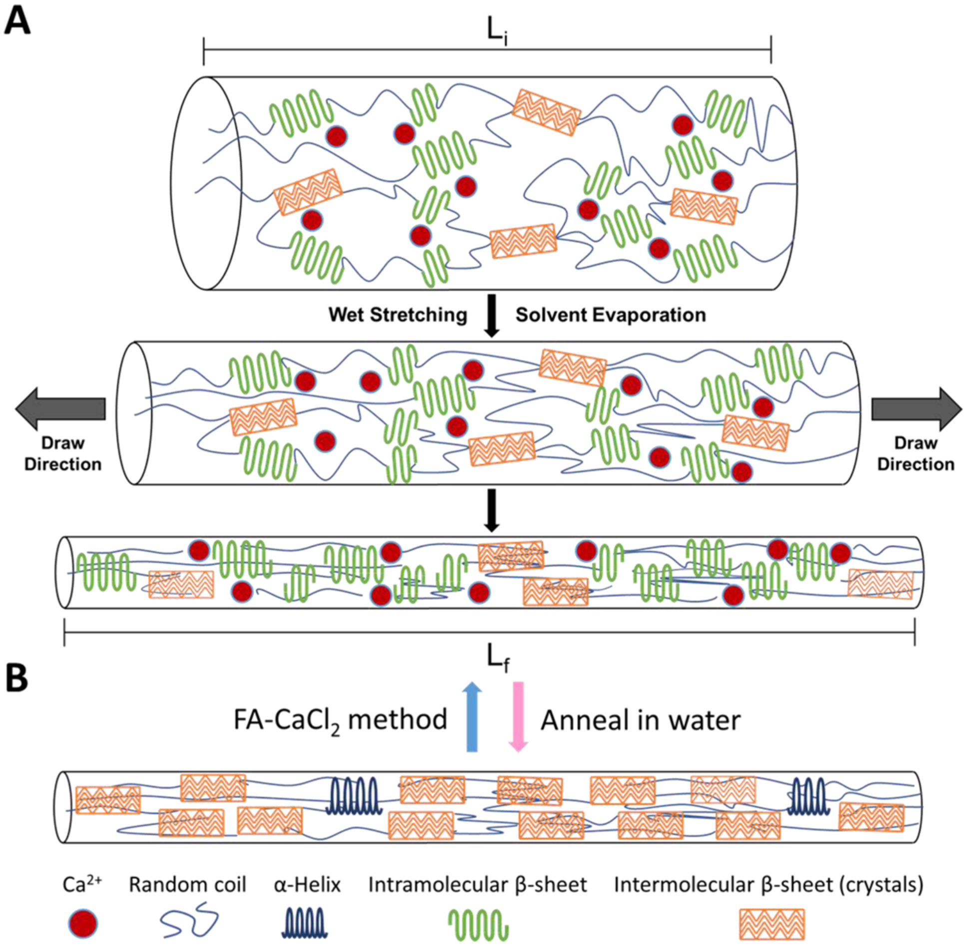

Figure 7. Proposed structure models of postdrawn SF nanofibers. (A) As the electrospun SF fibers are anchored on both ends and postdrawn, the reduction in diameter causes the amorphous and crystalline regions to arrange in parallel, such that large amounts of intramolecular *β*-sheets and small amounts of intermolecular *β*-sheets (crystals) are packed closely with connecting random coils that extended, leading to a higher degree of molecular orientation. (B) By removing $CaCl_2$ in water, the closely organized intramolecular *β*-sheets are induced into large amounts of intermolecular *β*-sheets (crystals) that form stable molecular interactions, causing a decrease in the mobility that results in a higher strength fiber.

postdrawing SF nanofibers could alter the protein chain arrangement into a more ordered structure, such as an intramolecular *β*-sheet structure. The table also summarizes the T_{d2} values of all SF nanofibers and film samples, with an order of random < DR1 < film < DR1.5 < DR2. The T_{d2} values of SF DR1.5 and DR2 nanofibers (273.15 and 273.65 °C, respectively) were found to be significantly higher than those of SF random and DR1 nanofibers, indicating that drawn nanofibers were more thermally stable than undrawn nanofibers, which is consistent with previous wet-spinning studies.[33]

Thermogravimetric analysis measurements were also conducted on the various SF nanofibers and film samples to evaluate how thermal stability can be affected by structural intermolecular interactions. The mass percentage changes and the first derivative thermogravimetry (DTG) curves are shown in Figure 6C,D. The thermal transition temperatures under increasing draw ratios are summarized in Figure 6E. The TGA and DTG curves can be divided into three subsequent regions characterized by their respective mass loss rates. From Figure 6C, there was no significant weight loss when the temperature was increased from 50 to 150 °C that is attributed to the solvent/water evaporation of bound molecules for all samples, as similar results were observed in the above DSC study (T_{d1}). After that, no significant mass losses between 150 and 280 °C were detected. At 280 °C, a fast decrease in mass was recorded for all samples until 400 °C, which is associated with thermal fibroin degradation. The bound solvent/water content (T_w), onset temperature of decomposition (T_d), middle degradation temperatures (T_{dm}), and remaining mass at 400 °C are shown in Figure 6D. A weight loss of about 9.8 ± 0.2% was detected around 50−150 °C for all samples associated with the evaporation of bound solvent/water. At 300 °C, the maximum weight loss for all samples was observed, with a difference of 15 °C between them. From Figure 6E, SF random samples had an earlier mass loss during the maximum degradation stages, compared to the aligned SF nanofibers (DR1) and film sample, with a T_{dm} trend of random < DR1 < film < DR1.5 < DR2. As the temperature is increased further to 400 °C, the mass residue started to level off, giving the remaining mass (%). At 400 °C, the SF random mesh samples had a remaining mass of about 24.58%, which was lower than the 26.71% mass residue content of the postdrawn SF nanofibers (DR2). Therefore, it was found that the SF-drawn nanofibers had higher thermal degradation temperatures and more remaining mass contents than undrawn samples. This implies that the SF intermolecular and intramolecular *β*-sheet contents can be induced and oriented through the postdrawing process, leading to higher thermal stability.

3. DISCUSSION

3.1. Fabrication Process. Recent efforts in tissue engineering, drug delivery, and short-term sensors and medical devices have drawn considerable attention toward new protein-based materials by taking advantage of silk's biocompatibility and biodegradability. Various bioinspired spinning approaches have been proposed, with priority on replicating the natural spinning system. The artificial spinning processes can be grouped into three categories: wet-spinning, drying spinning, and electrospinning. The most common technique to generate fibers is wet-spinning that initiate solidification via precipitation in a coagulation bath.[34] However, this preparation process is rather time- and energy-intensive and requires additional post-treatment processes that require large quantities of solvents that are expensive and highly toxic. In wet-spinning SF, a rapid conformation transition occurs as the concentrated fibroin solution enters the coagulating bath. While these fibers can be easily spun, the instantaneous assembly of the silk proteins can result in the formation of premature β-sheets and microvoids in the fibers when solvent molecules and salts are rapidly removed, resulting in lowered strength and toughness.[35] In addition, solutions pumped out by ejection from a glass capillary, hypodermic syringe, or microfluidic device will experience increased die swell, as increased extrusion pressure is needed to force the viscous fibroin solution through the spinneret, which can lead to defects and result in larger diameter fibers.[36] In contrast, dry spinning, a variation of the wet-spinning, is the process by which solidification of fibers occurs during the evaporation of the volatile solvent to a gaseous environment. The process is relatively low cost and simple to operate, resembling the natural spinning process in air. For example, high-performance regenerated silk fibers have been produced from highly concentrated nematic silk microfibril solutions and regenerated SF solutions, with direct extrusion into an open environment atmosphere.[37] With continuous extrusion, highly oriented uniform fibers can be collected. However, dry spinning is usually limited in the microscale and slow since the roller-reeling and winding apparatus used for the collections have reeling speeds of only 4−14 mm/s.[37] To produce artificial silk fibers in the nanoscale, electrospinning is a commonly used technique.[38] Protein-based nanofibers have good biocompatibility and minimal inflammatory responses. However, electrospun nanofibers possess weak mechanical properties, limiting applications for higher-performance structural materials. By implementing the automated TD technology in conjunction with electrospinning, SF nanofiber can be postdrawn simultaneously to enhance its mechanical properties. In addition, all processes can be implemented under physiological and ambient environmental conditions.

3.2. Postdrawing Mechanism. To explain the mechanical and thermal improvements of postdrawn SF nanofibers, a possible model was proposed in Figure 7 based on the experimental results. For this study, a calcium chloride and formic acid ($CaCl_2$−FA) solvent system has been used to produce regenerated SF solutions for electrospinning. Based on previous studies and investigations, it has been reported that the Ca^{2+} ions in the FA solution can directly disrupt and prevent the intermolecular hydrogen bonding in the intermolecular β-sheet crystals found in SF materials. The $CaCl_2$ molecules act as a plasticizer, which prevents hydrogen bonding and stacking of multilayer intermolecular β-sheet crystals, resulting in single-layer intramolecular β-sheets and increases in random coils.[17] As shown in Figure 7A, SF nanofibers regenerated from degummed silk fibers are intramolecular β-sheets dominated, with lesser amounts of intermolecular β-sheets. As the SF fibers are postdrawn (Figure 7B), the diameter decreases as large amounts of intramolecular β-sheets and small amounts of intermolecular β-sheets (crystals) linked by random coils come into close proximity and are aligned (bridged) as the fiber is extended. Since the presence of Ca^{2+} ions strongly disrupts the cross-linking and formation of intermolecular β-sheet crystals, the SF samples were water-treated to remove $CaCl_2$ and formic acid residues (after the drying process). Studies have shown that upon annealing in methanol/water solution, the structures of the organized intramolecular β-sheets are induced and transferred into large amounts of intermolecular β-sheets (crystals) to form stable molecular interactions resulting in a stronger fiber.[12,17,39]

3.3. Applications. The automated TD system has been made to imitate the natural pultrusion spinning of silkworms and translate the mechanism for guiding molecular assembly into high-performance materials. This new method has fewer processing steps, lower cost, and sustainable manufacturing of ultrathin SF fibers with controllable thickness, morphology, and molecular alignment. This offers new avenues of opportunity in the biomedical field, where tunable structural materials are needed for potential applications in tissue engineering and drug delivery.[40,41] These highly aligned silk nanofibers can be loaded with a variety of functional molecules, such as antibiotics, drugs, and enzymes, and be incorporated into a wide variety of fiber composite forms, such as films, sponges, tubes, and hydrogels, for unique applications such as high-performance and highly functional scaffolds, skin grafts, and composite devices. With this artificial spinning approach, polymorphic hierarchical SF-reinforced scaffolds can be built into complex 3D architectures via a layer-by-layer (LBL) approach.[42,43] In fiber-reinforced hydrogels, the embedded nanofibers can help retain and maintain the porous 3D hydrogel structure crucial for stem cell growth and differentiation.[44] In addition, SF nanofiber grafts and mats have shown to be a suitable temporary space for the retention and survival of adipose-derived MSCs.[45] Efforts in peripheral nerve regeneration have been made toward the development of nerve guide conduits (NGCs) for the attachment, growth, and contact guidance of nerve cells.[46,47]

4. CONCLUSIONS

In this work, it is demonstrated that the addition of a postdrawing stage with an automated track collector to the electrospinning process is a versatile and robust nanomanufacturing technique for the production of electrospun postdrawn protein nanofibers. Consequently, the postdrawing step resulted in the altered chemical bond composition and macromolecular alignment of fibrous protein chains and crystalline β-sheets, which improved the molecular orientation and mechanical properties of electrospun SF nanofibers. Analysis of polarized FTIR indicates that the C═O and C−N−H transition moments of drawn automated track SF fibers are more organized in the draw direction aligned to the fiber axis. With increasing draw ratio, the β-sheet crystallites were pulled and extended in the draw direction, illustrated by a systematic increase in molecular order parameter $\langle P_2 \rangle$, increases in glass-transition decomposition temperatures, increases in modulus, and reduction of max elongation. Young's modulus of SF nanofibers increased by 115%, and the ultimate tensile strength increased by 80% as a result of increased orientation via postdrawing up to a DR2. It is shown that the postdraw processing of electrospun regenerated fibers can lead to the production of enhanced tensile behavior of SF nanofibers in terms of increasing draw ratios, similar to wet-spinning, ascribed by the improved macromolecular and crystal alignment. In contrast to wet-stretching, postdrawing with an automated track collector has the ability to postdraw individual SF fibers in the nanoscale continuously, addressing disadvantages seen in electrospinning across a static parallel plate and conventional wet-spinning of silk microfiber production. We expect that the automated track design is compatible with other SF silkworm species, such as Thai, Eri, Muga, and Tussah, as well as other spider silks and fibrous proteins, which can be used in a wide variety of biomedical applications from regenerative wound dressing to flexible bioelectronic devices.[12,40] Furthermore, silks possess other useful material properties, such as high thermal conductivity for heat dissipation in smart textiles, optical transparency for applications in bio-optics, and enhanced mechanical strength for the 3D printing of monolithic structures in nanofiber-reinforced polymer composites. By offering an evolution-based manufacturing strategy for industrial protein manufacturing, silk can be artificially transformed into next-generation materials.

5. EXPERIMENTAL SECTION

5.1. Fabrication of Regenerated SF Nanofiber and Electrospinning Parameters. Raw *B. mori* silkworm cocoons were purchased from Treenway Silks (Lakewood, CO). In this work, the raw silk cocoons were first cut into pieces and degummed (boiled) two times in 0.02 M sodium bicarbonate ($NaHCO_3$) (Sigma-Aldrich) solution at 100 °C for 20 min and washed (rinsed) with Milli-Q water to remove (dissolved) the sericin coating from the surface of the silk fibers. The degummed SF fibers were then collected and air-dried for 48 h. After drying, the SF fibers were solubilized in a binary solvent system of formic acid (FA) (98%, Millipore Sigma-Aldrich) and 4% (w/w) calcium chloride ($CaCl_2$) (Sigma-Aldrich) with vigorous mixing (on a Vortex shaker) for 20 min, which yielded a final SF concentration of 15% (w/v). Before electrospinning, the regenerated SF solutions were centrifuged at 1000 rpm for 15 min to remove excess air bubbles from the previous shaking and loaded into a 5 mL syringe. For the spinning parameters, the solutions were then spun from a 21-gauge needle at an applied voltage of 13 kV, a needle-to-target distance of 12 cm (from the tip of the syringe to the top of the tracks), and a 0.05 mL/h feed speed. All as-spun and postdrawn SF nanofibers were electrospun in a custom, closed acrylic chamber housed in a fume hood. The environment inside the chamber had a temperature and relative humidity of 25 °C and 50%, respectively. Following previously established methods,[17,48,49] the SF samples were vacuum-dried at room temperature for 48 h to evaporate the residual solvent (formic acid) before water annealing treatment. To remove the $CaCl_2$ and any additional residual FA,[50] the SF samples were washed twice for 3 h and soaked in Milli-Q water for 24 h and dried again before analysis. Films were fabricated from the same solutions as electrospun nanofibers.

5.2. Morphological and Mechanical Characterization. The morphology of the SF nanofibers was observed using a Phenom Pure SEM instrument (Nanoscience Instruments, AZ). Images were analyzed using ImageJ software to determine fiber diameters. The surface morphology of post-treated regenerated SF nanofibers was observed using a Phenom Pure scanning electron microscopy (SEM: Nanoscience Instruments) at a 5 kV accelerating voltage. To improve the resolution of the images, all SF nanofibers were made electrically conductive by sputter coating a thin layer (covering) of gold using a Cressington 108 Auto Sputter Coater (Watford, England). Silk nanofiber samples were mounted on plastic film frames with a length of 10 mm in the fiber axis direction. The average number of fibers/sample perpendicular to the fiber axis and the average fiber diameter were measured from SEM images using ImageJ to calculate the estimated cross section of each individual sample. Thus, each sample used an independent cross section for stress calculations. The mechanical properties of the silk nanofibers and films were measured using a Shimadzu EZ-SX universal tensile tester (Kyoto, Japan) with a 2 N load cell at room temperature. The sides of the frame were cut after sample clamping and prior to tensile testing so that the silk fiber array resisted load independently. The gauge length and extension (cross-head) speed were fixed and set at 10 mm and 3 mm/min, respectively, for all measurements. Five independent measurements from each SF type were tested until sample failure, and the reported values were averaged. From the resultant stress−strain curves, the maximum load, Young's modulus, percentage extension at break, and yield stress were determined. Young's modulus was measured from the initial linear portion of the stress−strain curve.

5.3. Fourier Transform Infrared (FTIR) Spectroscopy. A Scientific IS50 Nicolet FTIR spectrometer (MA) was equipped with a standard KBr beamsplitter and an infrared ZeSe wire grid polarizer. The polarized FTIR was operated in transmission mode with 128 scans at a resolution of 4 cm^{-1} in the wavenumber range between 4000 and 400 cm^{-1}. For the polarization experiments, various collected mats of aligned SF nanofibers were irradiated with a polarized infrared beam parallel (0°) and perpendicular (90°) to the fiber axis.[51] The IR transmission spectra of the two polarization conditions were recorded, where parallel absorption ($A_{\parallel}$) was obtained by the electric vector direction of the polarized parallel (0°) IR beam and perpendicular absorption ($A_{\perp}$) was obtained by the electric vector direction of the polarized parallel (90°) IR beam. When the polarized electric field contacts the material, the peak intensity reaches its maximum when the chemical bonds reside or are oriented in the same direction.[51] Omnic spectra software (Thermo Fisher Scientific) was used to record the spectra and analyze the peak intensity of absorbance, after baseline correction and normalization, to determine the degree of macromolecular (polymer chain) orientation with the effect of postdrawing treatment at changing draw ratios. To find the degree of molecular orientation, dichroic ratios (R) of each band were calculated according to the following equation[23,52]

$$R = A_{\parallel}/A_{\perp} \tag{1}$$

where $A_{\parallel}$ and $A_{\perp}$ are the integrated absorbance of parallel (0°) and perpendicular (90°) peak intensities, respectively. As such, the values of $R > 1$ represent chemical bond absorbance oriented parallel to the fiber axis (or draw direction), and the values $R < 1$ represent chemical bond absorbance oriented perpendicular to the fiber axis, while the value of $R = 1$ reflects an isotropic material. The molecular order parameter $\langle P_2 \rangle$, or the orientation factor, was then calculated using R to determine the orientation correlation of the polymer chain backbone to the fiber axis (eq 2)[23,31]

$$\langle P_2 \rangle = (R - 1)/(R + 2) \tag{2}$$

For an isotropic material with no orientation, $\langle P_2 \rangle = 0$. While values close to $\langle P_2 \rangle = 1$ represent β-sheets that align perfectly parallel with polymer chain backbones with the fiber axis, such that the angle between the fiber axis and the C−N−H transition moment is near zero ($\sigma = 0°$). For values close to $\langle P_2 \rangle = -0.5$, β-sheets with polymer side chains reside perfectly perpendicular to the fiber axis, such that the angle between the fiber axis and the C═O transition moment is near $\sigma = 90°$.

5.4. Differential Scanning Calorimetry (DSC). Differential scanning calorimetry (DSC) measurements were performed on a TA Instruments DSC Q100 (TA Instruments, DE) with a refrigerated cooling system to examine the thermal behavior of SF nanofiber and film samples. Samples of 6 mg were cut (from fibers and films), encapsulated in an aluminum pan, and heated from −25 to 400 °C at a heating rate of 2 °C/min for standard mode DSC measurements under a nitrogen atmosphere with a flow rate of 50 mL/min, while temperature-modulated differential scanning calorimetry (TMDSC) tests were heated at an underlying heating rate of 2 °C/min with a modulation amplitude of 0.318 °C and a period of 60 s. The equipment was calibrated with an empty cell to form a baseline, an indium standard to characterize the temperature, and a sapphire reference standard to characterize the heat flow and heat capacity of the system.

5.5. Thermal Gravimetric Analysis (TGA). Thermogravimetric analysis (TGA) was carried out on a TA Instruments TGA Q600 (DE) to analyze the thermal stability of the SF nanofibers and film samples. The SF samples were cut, and weights of 12 mg were placed into ceramic pans before loading. The analysis was conducted under a continuous nitrogen purge of 50 mL/min from 25 to 600 °C with a heating rate of 5 °C/min. Universal Analysis software was used for data acquisition and processing.

5.6. Statistical Analysis. All reported standard deviations have been averaged over five ($n = 5$) independent measurements. The data are expressed as means ± standard errors of the mean, and statistical analysis was performed using statistical software OriginPro 8 (Originlab Corporation). Pairwise comparisons between groups and within groups were conducted using Mann−Whitney tests. A value of $P < 0.05$ was considered statistically significant.

ASSOCIATED CONTENT

Supporting Information

The Supporting Information is available free of charge at https://pubs.acs.org/doi/10.1021/acsabm.1c00630.

Schematic of polarized FTIR and examples of FTIR deconvolution (PDF)

AUTHOR INFORMATION

Corresponding Author

Vince Beachley − *Department of Biomedical Engineering, Rowan University, Glassboro, New Jersey 08028, United States*; orcid.org/0000-0001-8793-433X; Email: beachley@rowan.edu

Authors

Dave Jao − *Department of Biomedical Engineering, Rowan University, Glassboro, New Jersey 08028, United States*

Xiao Hu − *Department of Biomedical Engineering, Department of Physics and Astronomy, and Department of Molecular and Cellular Biosciences, Rowan University, Glassboro, New Jersey 08028, United States*; orcid.org/0000-0002-2579-2820

Complete contact information is available at: https://pubs.acs.org/10.1021/acsabm.1c00630

Notes

The authors declare no competing financial interest.

Raw and processed data is publically available in Mendeley Data: https://data.mendeley.com/datasets/j4g3wy3mz7/draft?a=ea38f6a6-aaae-4706-8e3d-e171f7b87d41.

ACKNOWLEDGMENTS

This study was supported by the National Science Foundation Materials Engineering and Processing Program (NSF1561966 and NSF1653329). X.H. was also supported by the NSF Biomaterials Program (DMR-1809541).

REFERENCES

(1) Qiu, W.; Patil, A.; Hu, F.; Liu, X. Y. Hierarchical Structure of Silk Materials Versus Mechanical Performance and Mesoscopic Engineering Principles. *Small* **2019**, No. 1903948.

(2) Aghaei-Ghareh-Bolagh, B.; Mithieux, S. M.; Hiob, M. A.; Wang, Y.; Chong, A.; Weiss, A. S. Fabricated tropoelastin-silk yarns and woven textiles for diverse tissue engineering applications. *Acta Biomater.* **2019**, *91*, 112−122.

(3) Ago, M.; Jakes, J. E.; Rojas, O. J. Thermomechanical properties of lignin-based electrospun nanofibers and films reinforced with cellulose nanocrystals: A dynamic mechanical and nanoindentation study. *ACS Appl. Mater. Interfaces* **2013**, *5*, 11768−11776.

(4) Guo, C.; Li, C.; Mu, X.; Kaplan, D. L. Engineering silk materials: From natural spinning to artificial processing. *Appl. Phys. Rev.* **2020**, *7*, No. 011313.

(5) Zhou, G.; Shao, Z.; Knight, D. P.; Yan, J.; Chen, X. Silk fibers extruded artificially from aqueous solutions of regenerated *Bombyx mori* silk fibroin are tougher than their natural counterparts. *Adv. Mater.* **2009**, *21*, 366−370.

(6) Jin, Y.; Zhang, Y.; Hang, Y.; Shao, H.; Hu, X. A simple process for dry spinning of regenerated silk fibroin aqueous solution. *J. Mater. Res.* **2013**, *28*, 2897.

(7) Sparkes, J.; Holland, C. Analysis of the pressure requirements for silk spinning reveals a pultrusion dominated process. *Nat. Commun.* **2017**, *8*, No. 594.

(8) Zhang, C.; Zhang, Y.; Luo, J.; Shi, J.; Shao, H.; Hu, X. Microstructural evolution of regenerated silk fibroin/graphene oxide hybrid fibers under tensile deformation. *RSC Adv.* **2017**, *7*, 3108−3116.

(9) Li, D.; Wang, Y.; Xia, Y. Electrospinning of polymeric and ceramic nanofibers as uniaxially aligned arrays. *Nano Lett.* **2003**, *3*, 1167−1171.

(10) Jao, D.; Beachley, V. Z. Continuous dual-track fabrication of polymer micro-/nanofibers based on direct drawing. *ACS Macro Lett.* **2019**, *8*, 588−595.

(11) Madurga, R.; Gañán-Calvo, A. M.; Plaza, G. R.; Guinea, G. V.; Elices, M.; Pérez-Rigueiro, J. Straining flow spinning: production of regenerated silk fibers under a wide range of mild coagulating chemistries. *Green Chem.* **2017**, *19*, 3380−3389.

(12) Wang, F.; Wolf, N.; Rocks, E.-M.; Vuong, T.; Hu, X. Comparative studies of regenerated water-based Mori, Thai, Eri, Muga and Tussah silk fibroin films. *J. Therm. Anal. Calorim.* **2015**, *122*, 1069−1076.

(13) Lu, Q.; Hu, X.; Wang, X.; Kluge, J. A.; Lu, S.; Cebe, P.; Kaplan, D. L. Water-insoluble silk films with silk I structure. *Acta Biomater.* **2010**, *6*, 1380−1387.

(14) Byler, D. M.; Susi, H. Examination of the secondary structure of proteins by deconvolved FTIR spectra. *Biopolymers* **1986**, *25*, 469−487.

(15) Oberg, K.; Chrunyk, B. A.; Wetzel, R.; Fink, A. L. Native-like secondary structure in interleukin-1. beta. Inclusion bodies by attenuated total reflectance FTIR. *Biochemistry* **1994**, *33*, 2628−2634.

(16) Seshadri, S.; Oberg, K. A.; Fink, A. L. Thermally denatured ribonuclease A retains secondary structure as shown by FTIR. *Biochemistry* **1994**, *33*, 1351−1355.

(17) Xue, Y.; Wang, F.; Torculas, M.; Lofland, S.; Hu, X. Formic Acid Regenerated Mori, Tussah, Eri, Thai, and Muga Silk Materials: Mechanism of Self-Assembly. *ACS Biomater. Sci. Eng.* **2019**, *5*, 6361−6373.

(18) Hu, X.; Lu, Q.; Sun, L.; Cebe, P.; Wang, X.; Zhang, X.; Kaplan, D. L. Biomaterials from ultrasonication-induced silk fibroin−hyaluronic acid hydrogels. *Biomacromolecules* **2010**, *11*, 3178−3188.

(19) Beachley, V.; Katsanevakis, E.; Zhang, N.; Wen, X. A novel method to precisely assemble loose nanofiber structures for regenerative medicine applications. *Adv. Healthcare Mater.* **2013**, *2*, 343−351.

(20) Berger, A. J.; Linsmeier, K. M.; Kreeger, P. K.; Masters, K. S. Decoupling the effects of stiffness and fiber density on cellular

behaviors via an interpenetrating network of gelatin-methacrylate and collagen. *Biomaterials* **2017**, *141*, 125−135.

(21) Callaway, K. A.; Xue, Y.; Altimari, V.; Jiang, G.; Hu, X. Comparative investigation of thermal and structural behavior in renewably sourced composite films of even-even nylons (610 and 1010) with silk fibroin. *Polymers* **2018**, *10*, No. 1029.

(22) Hu, X.; Kaplan, D.; Cebe, P. Determining beta-sheet crystallinity in fibrous proteins by thermal analysis and infrared spectroscopy. *Macromolecules* **2006**, *39*, 6161−6170.

(23) Zhang, X.; Gong, D.; Gong, Y. Insight into the orientation behavior of thermal-aged and historic silk fabrics by polarized FTIR microspectroscopy. *J. Cultural Heritage* **2019**, *38*, 53−63.

(24) Shen, Y.; Johnson, M. A.; Martin, D. C. Microstructural characterization of *Bombyx mori* silk fibers. *Macromolecules* **1998**, *31*, 8857−8864.

(25) Lefèvre, T.; Rousseau, M.-E.; Pézolet, M. Protein secondary structure and orientation in silk as revealed by Raman spectromicroscopy. *Biophys. J.* **2007**, *92*, 2885−2895.

(26) Hernández Cruz, D.; Rousseau, M.-E.; West, M. M.; Pézolet, M.; Hitchcock, A. P. Quantitative Mapping of the Orientation of Fibroin *β*-Sheets in B. m ori Cocoon Fibers by Scanning Transmission X-ray Microscopy. *Biomacromolecules* **2006**, *7*, 836−843.

(27) Xu, C.; Li, D.; Cheng, Y.; Liu, M.; Zhang, Y.; Ji, B. Pulling out a peptide chain from -sheet crystallite: Propagation of instability of H-bonds under shear force. *Acta Mech. Sin.* **2015**, *31*, 416−424.

(28) Hu, X.; Kaplan, D.; Cebe, P. Dynamic protein− water relationships during *β*-sheet formation. *Macromolecules* **2008**, *41*, 3939−3948.

(29) Garside, P.; Lahlil, S.; Wyeth, P. Characterization of historic silk by polarized attenuated total reflectance Fourier transform infrared spectroscopy for informed conservation. *Appl. Spectrosc.* **2005**, *59*, 1242−1247.

(30) Boulet-Audet, M.; Lefèvre, T.; Buffeteau, T.; Pézolet, M. Attenuated total reflection infrared spectroscopy: an efficient technique to quantitatively determine the orientation and conformation of proteins in single silk fibers. *Appl. Spectrosc.* **2008**, *62*, 956−962.

(31) Paquet-Mercier, F.; Lefèvre, T.; Auger, M.; Pézolet, M. Evidence by infrared spectroscopy of the presence of two types of *β*-sheets in major ampullate spider silk and silkworm silk. *Soft Matter* **2013**, *9*, 208−215.

(32) Zhou, W.; Chen, X.; Shao, Z. Conformation studies of silk proteins with infrared and raman spectroscopy. *Prog. Chem.* **2006**, *18*, No. 1514.

(33) Madurga, R.; Gañán-Calvo, A. M.; Plaza, G. R.; Atienza, J. M.; Guinea, G. V.; Elices, M.; López, P. A.; Daza, R.; González-Nieto, D.; Pérez-Rigueiro, J. Comparison of the effects of post-spinning drawing and wet stretching on regenerated silk fibers produced through straining flow spinning. *Polymer* **2018**, *150*, 311−317.

(34) Pérez-Rigueiro, J.; Madurga, R.; Gañán-Calvo, A. M.; Plaza, G. R.; Elices, M.; López, P. A.; Daza, R.; González-Nieto, D.; Guinea, G. V. Straining flow spinning of artificial silk fibers: A review. *Biomimetics* **2018**, *3*, No. 29.

(35) Yan, J.; Zhou, G.; Knight, D. P.; Shao, Z.; Chen, X. Wet-spinning of regenerated silk fiber from aqueous silk fibroin solution: discussion of spinning parameters. *Biomacromolecules* **2010**, *11*, 1−5.

(36) Peng, Q.; Zhang, Y.; Lu, L.; Shao, H.; Qin, K.; Hu, X.; Xia, X. Recombinant spider silk from aqueous solutions via a bio-inspired microfluidic chip. *Sci. Rep.* **2016**, *6*, No. 36473.

(37) Ling, S.; Qin, Z.; Li, C.; Huang, W.; Kaplan, D. L.; Buehler, M. J. Polymorphic regenerated silk fibers assembled through bioinspired spinning. *Nat. Commun.* **2017**, *8*, No. 1387.

(38) Yao, C.; Li, X.; Song, T.; Li, Y.; Pu, Y. Biodegradable nanofibrous membrane of zein/silk fibroin by electrospinning. *Polym. Int.* **2009**, *58*, 396−402.

(39) Hu, X.; Kaplan, D.; Cebe, P. Effect of water on the thermal properties of silk fibroin. *Thermochim. Acta* **2007**, *461*, 137−144.

(40) Chouhan, D.; Chakraborty, B.; Nandi, S. K.; Mandal, B. B. Role of non-mulberry silk fibroin in deposition and regulation of extracellular matrix towards accelerated wound healing. *Acta Biomater.* **2017**, *48*, 157−174.

(41) Chen, S.; Boda, S. K.; Batra, S. K.; Li, X.; Xie, J. Emerging roles of electrospun nanofibers in cancer research. *Adv. Healthcare Mater.* **2018**, *7*, No. 1701024.

(42) Mu, X.; Fitzpatrick, V.; Kaplan, D. L. From Silk Spinning to 3D Printing: Polymer Manufacturing using Directed Hierarchical Molecular Assembly. *Adv. Healthcare Mater.* **2020**, No. 1901552.

(43) Beachley, V.; Katsanevakis, E.; Zhang, N.; Wen, X. A novel method to precisely assemble loose nanofiber structures for regenerative medicine applications. *Adv. Healthcare Mater.* **2013**, *2*, 343−351.

(44) Beachley, V.; Wen, X. Fabrication of nanofiber reinforced protein structures for tissue engineering. *Mater. Sci. Eng. C* **2009**, *29*, 2448−2453.

(45) Wu, S.; Wang, Y.; Streubel, P. N.; Duan, B. Living nanofiber yarn-based woven biotextiles for tendon tissue engineering using cell tri-culture and mechanical stimulation. *Acta Biomater.* **2017**, *62*, 102−115.

(46) Wang, C.-Y.; Zhang, K.-H.; Fan, C.-Y.; Mo, X.-M.; Ruan, H.-J.; Li, F.-F. Aligned natural−synthetic polyblend nanofibers for peripheral nerve regeneration. *Acta Biomater.* **2011**, *7*, 634−643.

(47) Wang, L.; Wu, Y.; Hu, T.; Ma, P. X.; Guo, B. Aligned conductive core-shell biomimetic scaffolds based on nanofiber yarns/hydrogel for enhanced 3D neurite outgrowth alignment and elongation. *Acta Biomater.* **2019**, *96*, 175−187.

(48) Liu, Q.; Wang, F.; Gu, Z.; Ma, Q.; Hu, X. Exploring the structural transformation mechanism of chinese and Thailand silk fibroin fibers and formic-acid fabricated silk films. *Int. J. Mol. Sci.* **2018**, *19*, No. 3309.

(49) Zhang, F.; Yang, R.; Zhang, P.; Qin, J.; Fan, Z.; Zuo, B. Water-Rinsed Nonmulberry Silk Film for Potential Tissue Engineering Applications. *ACS Omega* **2019**, *4*, 3114−3121.

(50) Hietala, J.; Vuori, A.; Johnsson, P.; Pollari, I.; Reutemann, W.; Kieczka, H. *Ullmann's Encyclopedia of Industrial Chemistry: Formic Acid*; Wiley-VCH Verlag GmbH & Co., 2016; pp 1−22.

(51) Brennan, D. A.; Shirvani, K.; Rhoads, C. D.; Lofland, S. E.; Beachley, V. Z. Electrospinning and post-drawn processing effects on the molecular organization and mechanical properties of polyacrylonitrile (PAN) nanofibers. *MRS Commun.* **2019**, *9*, 764−772.

(52) Marsh, D. Dichroic ratios in polarized Fourier transform infrared for nonaxial symmetry of beta-sheet structures. *Biophys. J.* **1997**, *72*, 2710−2718.